Eurographics Symposium on Geometry Processing 2016
Maks Ovsjanikov and Daniele Panozzo
(Guest Editors)

Volume 35 (2016), Number 5

Data-Driven Bending Elasticity Design by Shell Thickness

Xiaoting Zhang[1,3†] Xinyi Le[2,3†] Zihao Wu[3] Emily Whiting[1] Charlie C.L. Wang[4,3]

[1]Dartmouth College [2]Shanghai Jiao Tong University [3] The Chinese University of Hong Kong [4] TU Delft

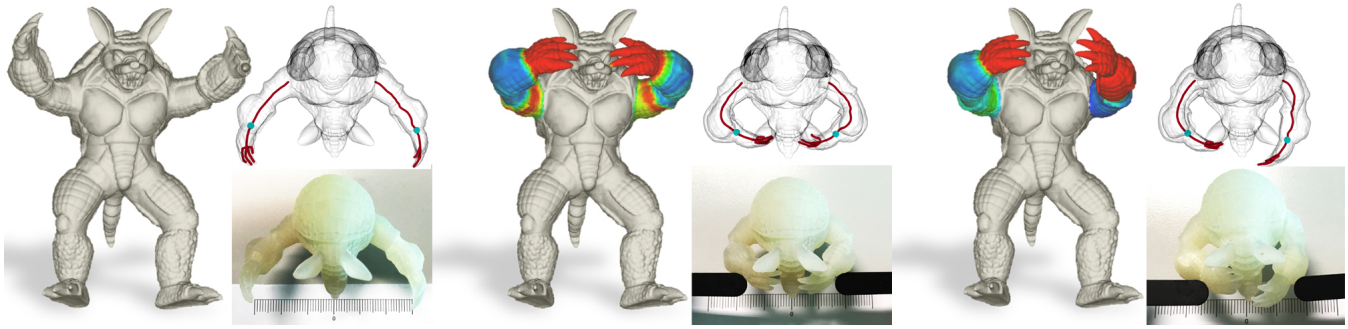

Figure 1: *Our work provides a design tool to realize the desired bending elasticity of a generalized cylindrical model by changing the shell thickness (blue=thin, red=thick). Given the shape of the model's rotational symmetry axis under bending, we use a data-driven method to compute a non-uniformly hollowed shape to realize the desired deformation behavior. The model is fabricated by 3D printing using a single material. (Left) Original pose; (Middle and Right) Two bending behaviors.*

Abstract

We present a method to design the deformation behavior of 3D printed models by an interactive tool, where the variation of bending elasticity at different regions of a model is realized by a change in shell thickness. Given a soft material to be used in 3D printing, we propose an experimental setup to acquire the bending behavior of this material on tubes with different diameters and thicknesses. The relationship between shell thickness and bending elasticity is stored in an echo state network using the acquired dataset. With the help of the network, an interactive design tool is developed to generate non-uniformly hollowed models to achieve desired bending behaviors. The effectiveness of this method is verified on models fabricated by different 3D printers by studying whether their physical deformation can match the designed target shape.

Categories and Subject Descriptors (according to ACM CCS): I.3.5 [Computer Graphics]: Computational Geometry and Object Modeling—Physically based modeling; J.6 [Computer-Aided Engineering]: Computer-aided design (CAD)—

1. Introduction

The rapid development of digital fabrication through 3D printing has enabled fast prototyping of customized designs for individuals and manufacturers. The ability to use elastic material in 3D printing opens the door for fabricating deformable objects, such as customized toys, gadgets and soft robotics. Whether designed for functional usage or entertainment, such objects are expected to deform in a particular, desired manner. Unfortunately, it is complicated and counterintuitive to design the deformation behavior of a 3D printed elastic object [CZXZ14]. Moreover, since most of the additive manufacturing technologies are restricted to a very small set of materials, adjusting the structure of the object may be the only way to achieve the desired deformation behavior [SBR*15].

Different types of external forces can be grouped into five fundamental loads: *bending, compression, shear, tension* and *torsion* [CSS06]. Among these, bending is the one that results in the largest visible change of shapes. In this paper, we tackle the problem of designing the bending behavior of 3D printed models. Our work focuses on generalized cylindrical shapes, since bending mainly occurs on these beam-like shapes. A data-driven approach is developed to apply the bending behavior learned from primitive shapes (i.e., 3D printed tubes in different diameters/thicknesses) to models

† joint first author

with complex shapes. As a result, when fabricated by the same 3D printer with the same material used in data acquisition, the model's bending elasticity can be realized in a designed way (see Fig.1).

Our work is motivated by the recent developments in digital material design and fabrication. Approaches have been developed to design deformation behavior by (i) controlling the distribution of materials with different stiffness [STC*13, XLCB15] or (ii) using the combination of small structures in different patterns [SBR*15, PZM*15, BBO*10]. The first group of techniques are restricted to multi-material 3D printers, while the latter approaches result in a bumpy appearance for the fabricated models. To address these issues, we propose to design and fabricate the desired deformation behavior by varying the model's shell thickness, avoiding changes to the appearance of the model and allowing fabrication by single-material 3D printers.

Prior approaches usually conduct *finite element method* (FEM) analysis to simulate the deformation behavior when optimizing the shape of a given model for desired behavior [BKS*12, STC*13, XLCB15, CLSM15]. However, FEM based shape modeling works in a trial and error way requiring experienced designers and a fixed setup with known external loads. We provide an alternative solution to calculate the relative thickness distribution where users focus only on the target shape without knowing the exact loads. Further, unlike FEM, the time-intensive work is offloaded to the pre-processing step so that users can design the target shape interactively without iterative calculations. Specifically, we propose a data-driven framework to determine the relationships between bending elasticity, shell thickness, and cross-section dimensions. We develop an interactive design tool to generate non-uniformly hollowed models that provide the desired behaviors under bending (e.g. Fig.1), and verify the effectiveness of our approach by printing the models using elastic materials.

Our approach Given a model in rest pose, our method first extracts its 1D curve skeleton referred to as medial representations. The user may then drag the skeleton into a new shape, indicating the shape of the fabricated model when pinning the endpoint of the skeleton at the target position. The challenge in creating such a design interface is determining the thicknesses at different regions on the given model to match the desired bending behavior. In this paper, we propose a data-driven approach to construct an explicit function that computes the distribution of shell thicknesses according to a designed bending behavior. As shown in Fig.2, our framework consists of three parts:

- *Data acquisition:* In this preprocessing step, cylindrical tubes with different diameters and thicknesses are fabricated by 3D printing. All tubes with the same length are deformed in a bending test with the same loading while forces at the end of the tubes are measured and controlled. Images of the deformed shapes are captured and the maximal deflection of the medial axis is measured at each sample.
- *Learning:* This is an offline computation step, where the nonlinear relationship between the deflection of the medial-axis, shell thickness and dimension of cross-sections are learned from the acquired data-set by the *echo state network* (ESN). The learning result is a simplified physical model for the tested material, represented by an explicit function for the thickness with desired deflection and cross-section dimensions as parameters.
- *Shape modeling:* The shape of the non-uniformly hollowed model is generated in this final step. With the help of the thickness function learned from acquisition, the thickness at scattered surface points is computed according to the virtual cross-sections. After generating the continuous distribution of thicknesses via diffusion over the entire surface, the final result of hollowing can be produced with the help of a shifted distance-field.

Contributions In summary, our contributions include (i) a simplified physical model that efficiently predicts the change of bending elasticity on hollowed general cylindrical models, (ii) a novel data-driven framework to design bending elasticity on such models using the variation of shell thickness, and (iii) an interactive design tool to compute non-uniformly hollowed shapes to achieve user-specified bending behaviors. Note that, as the method only changes the interior surface of a hollowed model, the appearance of the design input is preserved.

2. Related Work

Simulations of deformation behavior have been widely used in computer graphics. Significant effort has been spent on the methodology of material parameter estimation so that the deformation behavior can be controlled. To speed up computation, reduced models are used in interactive applications. Recently, there is a trend to optimize the design for a variety of means of fabrication. We review the most related work in deformation control, reduced model and computational fabrication below, comprehensive reviews can be found in [NMK*06, SB12, LSWW14].

Material parameters are important to control deformation behavior in many applications. However, parameter estimation is often complex and it is impractical to tune manually (especially for non-linear or inhomogeneous materials). To overcome this difficulty, data-driven approaches have been developed to capture complex physical phenomena and material parameters in applications like cloth behavior [WHRO10, MBT*12, DASTH10], elastic deformation [MTGG11, PLR*16], soft tissue [WWY*15, STC*12] and fluid simulation [JSP*15]. Bickel et al. [BBO*09] design a modeling technique to simulate non-linear materials by estimating and interpolating the parameters of a material from measurements of real objects. They design and fabricate objects consisting of stacked layers from a small set of base materials, producing a composite that matches the desired forces and displacements [BBO*10]. Wang et al. [WOR11] propose a piecewise-linear elastic cloth model with parameters fitted from in-plane stretching and bending behaviors using gravity as the external forces. Other algorithms have been proposed for achieving target shapes under known loads by optimizing the rest shape [STC*13, CZXZ14]. All of these approaches employ a time-consuming physical simulation as the inner loop of optimization. In contrast, our approach uses a machine learning method to create a function that describes the relationship between multiple physical parameters.

For fast simulation, model reduction has been widely used in computer graphics (e.g., [KMOD09, KJ09, HSTP11, XLCB15]).

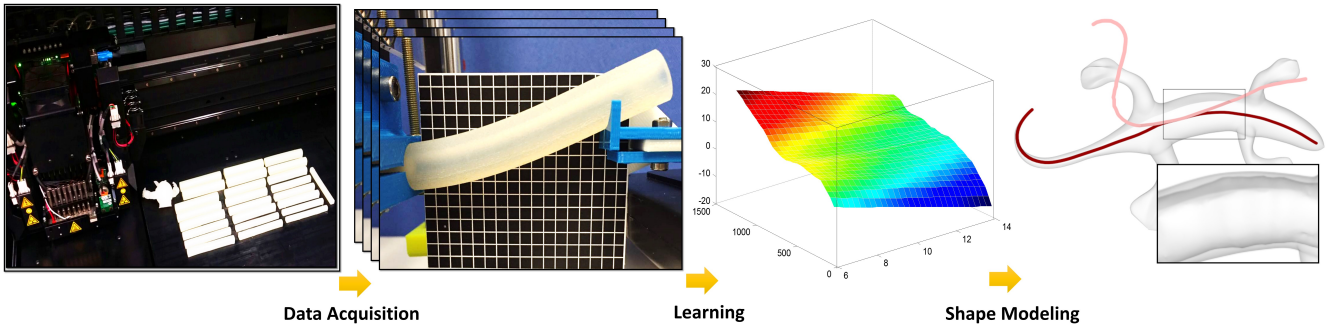

Figure 2: *Overview of our data-driven framework consisting of data-acquisition, learning and shape modeling.*

Recently, Umetani et al. [UKSI14] proposed a simplified aerodynamic model to optimize the designing of hand-launched free-flight glider airplanes. Inspired by this work, we develop a simplified physical model to describe the relationship between shell thickness and bending elasticity. Deformation effects at an object scale have also been approximated by an assembly of small-scale microstructures which are usually a number of patterns consisting of a base set [PZM*15, SBR*15]. When designing the deformation behavior by the microstructures, reduced models are often employed. This strategy provides an efficient way to control elasticity on models fabricated by 3D printing. However, appearance of the original model cannot be preserved as many holes are generated when using microstructures to design the elasticity of a printed model. Similar problems happen in [PTC*15], where the flexibility of a model is realized by a network of linked rods with different diameters. We do not suffer from the problem of appearance damage as the bending elasticity is designed in our framework by interior non-uniform hollowing.

Recently, many methods have been developed to optimize different aspects of models fabricated by 3D printing, including mechanical properties, manufacturing cost and appearance. Critical stress of models are detected and relieved by shape correction in [SVB*12, US13]. Lu et al. [LSZ*14] introduce an optimization algorithm for re-shaping interior structures of a model to relieve the internal stress. To reduce material volume, Wang et al. [WWY*13] designed a skin-frame structure which keeps the geometric shape and physical stable. Prévost et al. [PWLSH13] perform balance optimization to improve stability of printed objects. Several methods facilitate fabrication for desired appearance by different means – for example by mapping color textures to 3D surfaces using inkjet printers [ZYZZ], by scattering multiple materials [DLG13, HFM*10], or by avoiding artifacts caused by adding support structures in fabrication [ZLP*15]. Methods have also been developed to achieve desired reflectance [WPMR09, MAG*09, LDPT13]. Musialski et al. [MAB*15, MHR*16] provide generic paradigm for non-linear shape optimization for fabrication problems.

3. Bending Elasticity

The Euler-Bernoulli beam theory (also known as classical beam theory [FLS69]) is widely used in mechanical and civil engineering to govern the design of structures under bending deformation. It is a simplification of linear theory of elasticity that provides a method to calculate the deflection characteristics of beams under different loads in an algebraic way.

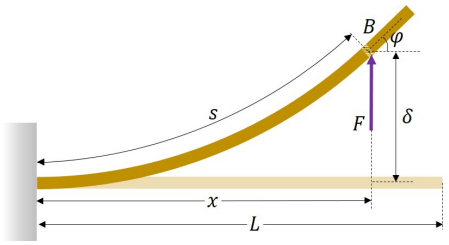

Figure 3: *An illustration for bending elasticity estimation by using the Euler-Bernoulli beam theory.*

Linear Beam Under the assumption of small deflection, the governing equation of beam theory is:

$$\frac{d^2}{dx^2}\left(EI\frac{d^2\delta}{dx^2}\right) = q(x), \tag{1}$$

where E is the Young's modulus of the material, I is the moment of inertia of the beam about the neutral axis, and $q(x)$ specifies the distribution of applied loads. For a cantilever beam with uniform cross-section under a concentrated load F at the position B with distance to wall x, the deflection δ at point B can be calculated as:

$$\delta = \frac{Fx^2}{6EI}(3L - x). \tag{2}$$

And the angle of rotation at point B is:

$$\varphi = \frac{Fx^2}{2EI}, \tag{3}$$

which is also called a *slope angle*.

Metric of Elasticity To evaluate the relative bending elasticity at different regions of a model, we simplify the problem by considering that uniform bending loads are applied everywhere so that global bending can be approximated by local deformations. The ease with which a beam is deformed under bending can be measured by a local scalar that is independent of length and external

loads:

$$M_\varphi = \frac{\varphi}{s}, \tag{4}$$

which is the slope angle under a unit arc length s. Under a fixed condition (i.e., the same F, E and x) the deflection and slope angle only depend on the value of I, which for a uniformly hollowed cylinder is:

$$I = \frac{\pi}{64}(D^4 - (D-2t)^4) \tag{5}$$

with D and t being the diameter of cylinder and the thickness of hollowing respectively. It is easy to show that the flexibility of a beam is increased by a smaller thickness t – i.e., producing a larger δ and φ with the same F.

Challenges The above formulas for deflection and slope angle assume a small deformation. A different governing equation should be applied when a large rotation occurs [HB00]:

$$EI\frac{d^4\delta}{dx^4} - \frac{3}{2}EA\left(\frac{d\delta}{dx}\right)^2\left(\frac{d^2\delta}{dx^2}\right) = q(x) \tag{6}$$

with A the area of cross-section, δ the deflection and $q(x)$ the distribution of loads. As a consequence, the nonlinear relationship under large rotation is hard to be derived into a simple form as Eq.(3). We can only conclude that the metric of bending elasticity on a beam, M_φ, is a function of D and t. In our approach, a data-driven strategy is employed to learn the nonlinear relationship between M_φ, D and t, where an explicit function of thickness $t(\cdot)$ is produced to control the relative elasticity of bending.

4. Data-Driven Modeling

In this section, we propose a data-driven approach to overcome the aforementioned challenges.

4.1. Data Acquisition

As shown in the left-most image of Fig.2, samples of uniformly hollowed tubes with the same length (100mm in our tests) are first fabricated by 3D printing. To span the range of shapes we wish to fabricate, we generated 45 tubes with diameters ranging from 6mm to 14mm and with thicknesses ranging from 1mm to 6mm. Among these samples, 25 tubes were spaced uniformly across D and t, while the dimensions of the remaining 20 were randomly assigned (see Fig.4). The reasonable minimal/maximal thickness of hollowing ($t_{\min}$ and $t_{\max}$) can be obtained through experimental tests.

After getting the fabricated samples, their bending elasticities are tested on a setup for experimental tests as shown in Fig.4. Our setup consists of a vise, a touching platform, a compression force sensor and a vertical movement frame with two screws, where a tube is locked by the vise during tests. The vise is installed on the frame and can be vertically driven by the screws. The other end of a tube is freely touched by the platform attached to the force sensor. By moving the vise down, the tube is bent and the force at the free end can be measured.

To measure the same load on each sample, we move the vise vertically until a constant force is measured at the free end of the tube. $F = 0.373N$ is applied in our tests, which agrees with general range of forces applied by human beings. The distance between the side walls of the vise and the platform is fixed in all test (i.e., x in Fig.3). The deflection, δ, on each sample can be can be read from the caliber. The slope angle, φ, can also be obtained from photos by measuring the bending angle of the tube's medial axis. Given δ and x, the arc-length s of a bended tube can be calculated by assuming the curve as a circular arc. Therefore, the metric of bending elasticity of each sample can be obtained by Eq.(4).

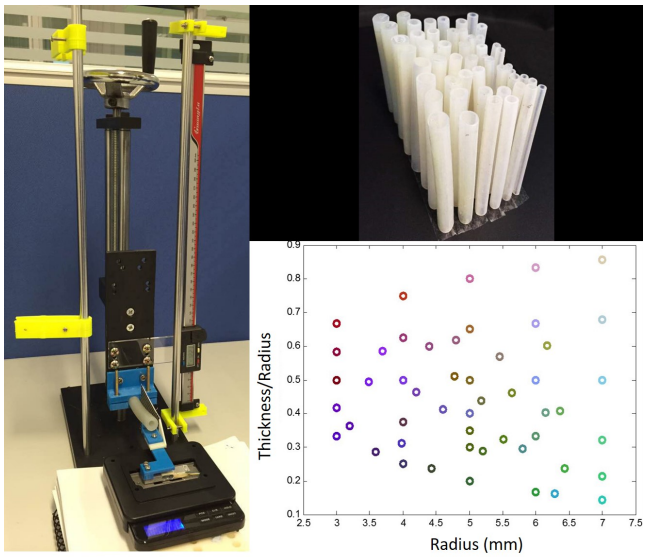

Figure 4: *Data-acquisition is taken on a experimental setup (left) with force sensors and fixtures. (right) Sample tubes with different diameters and thicknesses.*

With the set of training data, $\{D_i, t_i, M_i\}_{i=1,\ldots,m}$, the physical model to govern the design of bending elasticity will be constructed as a function $t(\cdot)$ that satisfies the equation

$$t(D_i, M_i) = t_i \quad (i = 1, \ldots, m). \tag{7}$$

As the governing equation of bending in large rotation is a high-order ODE (Eq.(6)), it is hard to derive an explicit form of $t(\cdot)$, even in its basic form. Therefore, we construct the function by a machine learning process below. The constraint on $t_{\min}$ and $t_{\max}$ can be integrated into the formulation as follows.

$$\begin{aligned} &t(D, M_\varphi) = t_{\min} + F(D, M_\varphi) \\ &s.t. \quad 0 < F(D, M_\varphi) < (t_{\max} - t_{\min}) \end{aligned} \tag{8}$$

We then learn the function $F(\cdot)$ by the training set $\{D_i, t_i, M_i\}$.

4.2. Learning by ESN

The function $F(\cdot)$ to be learned in our problem has its own characteristics, including highly nonlinear, low dimensional and small-sized. Moreover, the range of $F(\cdot)$ should be constrained. According to our problem, We employ *echo state network* (ESN) to learn the function. Echo state network has been widely applied in many

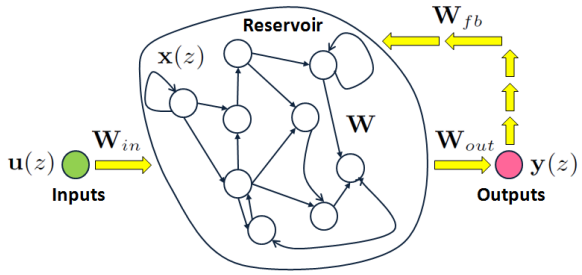

$\mathbf{u}(z)$	k-dimensional input signal
$\mathbf{y}(z)$	d-dimensional output signal
$\mathbf{x}(z)$	n-dimensional system state (called *reservoir*)
$\mathbf{W}$	$n \times n$ reservoir weight matrix
$\mathbf{W}_{in}$	$k \times n$ input weight matrix
$\mathbf{W}_{out}$	$d \times (k+n)$ output weight matrix
$\mathbf{W}_{fb}$	$n \times d$ output feedback matrix

Figure 5: *Illustration of Echo State Network*

practical training problems (ref. [SSW*13, LYS11]). Compared to other learning methods, ESN has following good characteristics. First, ESN is able to be learned from a small set of samples [Jae02]. Second, ESN has the short-term memory which uses a large "reservoir" recurrent neural network to produce desired combined output results [Jae01]. Thirdly, the structure of ESN is very simple so that we can easily add engineering constraints to meet our learning demands (e.g., the range constraint of thickness is added into the training model in our approach). Finally, the implementation of ESN can be greatly accelerated by using GPU [KW13].

Basically, ESN provides an architecture and supervised learning principle for *recurrent neural networks* (RNNs). As illustrated in Fig.5, the core of ESN is a set of n neurons with a random but fixed connectivity – described by a reservoir weight matrix $\mathbf{W}$. The more number of neurons are employed in the network, the more stable results can be obtained after training. In our implementation, we choose the parameters as $np = 10$ (the learning reservoir size is $n = 1{,}000$ and sparse connection rate is $p = 0.01$) to achieve a good balance between stability and efficiency. An input signal $\mathbf{u}(z)$ at discrete time z are linked to the neurons by a fixed input weight matrix, $\mathbf{W}_{in}$. Meanwhile, the state of neurons is represented by a vector $\mathbf{x}(z)$, which is bi-directionally connected to the d-dimensional output signal $\mathbf{y}(z)$ by $\mathbf{W}_{out}$ and $\mathbf{W}_{fb}$. Denote system state $\mathbf{z}(z) = [\mathbf{x}(z); \mathbf{u}(z)]$, the output signal $\mathbf{y}(z)$ is determined in ESN by

$$\mathbf{y}(z) = \mathbf{W}_{out}\mathbf{z}(z). \tag{9}$$

with a $d \times (k+n)$ output weight matrix, $\mathbf{W}_{out}$. If there's a new signal $\mathbf{u}(z+1)$ as input, the new system state $\mathbf{x}(z+1)$ is updated by it together with the system state and the output in last time step (i.e., $\mathbf{x}(z)$ and $\mathbf{y}(z)$). Details can be found in [Jae01].

When training ESN by a set of samples, different samples in the training set are considered as signals occurring at different discrete time steps. m samples of (D_i, M_i) obtained in our data acquisition step are considered as input signals generated at m time steps. The system state of neurons, $\mathbf{x}(z)$, and the output weight matrix, $\mathbf{W}_{out}$ are optimized to let input/output signals fulfill the constitutive equation. Define $\mathbf{Z} = [\mathbf{z}(1), \mathbf{z}(2), \ldots, \mathbf{z}(m)]$ as the collection matrix of extended system states and $\hat{\mathbf{Y}}$ as a $k \times d$ matrix indicating the desired output signals (i.e., the row vector of thicknesses $\mathbf{b} = \{t_i\}$ in our problem as $d = 1$), the system output matrix $\mathbf{W}_{out}$ can be determined by a linear regression as

$$\min \|\mathbf{W}_{out}\mathbf{Z} - \mathbf{b}\|^2. \tag{10}$$

Therefore, it can be computed by $\mathbf{W}_{out} = (\mathbf{Z}^{\dagger}\mathbf{b})^T$ with the pseudo-inverse of $\mathbf{Z}$ (denoted by $\mathbf{Z}^{\dagger}$). With the help of ESN-based learning, the thickness function $t(\cdot)$ can be estimated by the set of sample data.

Using the form of function in Eq.(8), the function $F(\cdot)$ is to be trained by the set of samples as $\{D_i, M_i, t_i - t_{\min}\}$. The constraint $F(\cdot) \in [0, r]$ with $r = t_{\max} - t_{\min}$ can be imposed by converting Eq.(10) into a convex optimization problem. Specifically, the update equation for system state in ESN,

$$\mathbf{x}(z+1) = f(\mathbf{W}\mathbf{x}(z) + \mathbf{W}_{in}\mathbf{u}(z+1) + \mathbf{W}_{fb}\mathbf{y}(z)) \tag{11}$$

can ensure $\mathbf{x}(z) \in (0,1)$ when using a sigmoid function, $f(\tau) = 1/(1+e^{-\tau})$, as the activation function. After scaling the input signals into $\{D_i/D_{\max}, M_i/M_{\max}\}$ by the maximal diameter and flexibility allowed in our framework, all components in the extended system state vector $\mathbf{z}(z)$ fall in the interval of $(0,1)$. Therefore, if $w_{a,b} \in (0, r/(k+n))$ ($\forall w_{a,b} \in \mathbf{W}_{out}$), the range of every component in the output signal (by Eq.(9)) can be guaranteed in the range of $[0, r]$. In summary, the output weight matrix $\mathbf{W}_{out}$ can be obtained by

$$\begin{aligned} &\min \|\mathbf{W}_{out}\mathbf{Z} - \mathbf{b}\|^2 \\ &s.t. \quad 0 < w_{a,b} < \frac{r}{k+n} \quad (\forall w_{a,b} \in \mathbf{W}_{out}) \end{aligned} \tag{12}$$

which is a convex optimization problem.

By this enhanced formulation of regression in ESN, the function $F(\cdot)$ generated by ESN-based learning can satisfy the range constraint in Eq.(8) – thus also the thickness function $t(\cdot)$.

5. Computation

In this section, the computation of thicknesses for designing bending elasticity is generalized to freeform models. As our design tool allows users to specify a desired behavior of skeletal deformation in bending, we first generate the skeleton for an input model. Then, the virtual cross-sections for points on the skeleton are constructed to help assign thicknesses on surface points of H. Lastly, a shifted distance-field is employed to generate the interior surface for non-uniform hollowing.

5.1. Virtual Cross-section

The skeleton $\mathcal{S}$ and virtual cross-sections of an input model $\mathcal{H}$ are generated by the *rotational symmetry axis* (ROSA) technique [TZCO09, ZYH*15]. We also follow the assumption of [TZCO09] on generalized cylindrical regions to be the shapes of interest. For a point $\mathbf{p}$ on the surface of $\mathcal{H}$, the algorithm starts from an initial cutting plane passing through $\mathbf{p}$. An iterative method is adopted to update the orientation of this cutting plane based on the normal of

neighboring regions that intersect with the cutting plane. The iteration stops when the cutting plane converges into a ROSA plane $\mathcal{P}(\mathbf{p})$, the normal of which is most perpendicular to the surface normals at the intersected points between $\mathcal{P}(\mathbf{p})$ and the surface of $\mathcal{H}$. A point on $\mathcal{P}(\mathbf{p})$ is also computed as ROSA point that minimizes the sum of squared distances to the line extensions of normals at the intersected points. Linking ROSA points generated by surface sample points can form a 1D skeleton $\mathcal{S}$ that is most rotationally symmetric about $\mathcal{H}$ at each segment.

In our framework, the skeleton $\mathcal{S}$ is used as a handle for designing the bending behavior. $\mathcal{S}$ is first sampled into a set of points $\{\mathbf{s}_1, \mathbf{s}_2, \ldots, \mathbf{s}_l\}$, which can be dragged to form a new shape of $\mathcal{S}$. The new position of $\mathbf{s}_j$ is denoted by $\hat{\mathbf{s}}_j$. The ROSA planes passing through each sample are then constructed (denoted by $\mathcal{P}(\mathbf{s}_j)$). The intersection between a ROSA plane $\mathcal{P}$ and $\mathcal{H}$ is computed and represented as sample points (see cyan curves shown in Fig.6). Note that intersection points located on other branches of $\mathcal{H}$ must be excluded. The remaining sample points represent the shape of a cross-section $\mathcal{C}(\mathbf{s}_j)$ passing through the skeleton point $\mathbf{s}_j$. In the following computation, each cross-section is locally considered as a cylinder when radius being the minimal distance between the $\mathcal{C}(\mathbf{s}_j)$'s boundary and the skeleton point $\mathbf{s}_j$. This is because bending deformation always occurs towards the weakest direction (i.e., the thinnest place).

5.2. Thickness Estimation and Diffusion

As each virtual cross-section $\mathcal{C}$ is locally considered as a cylinder, we can also analyze its bending flexibility according to the desired bending behavior given by designers (i.e., M_φ). For a point $\mathbf{s}_i$ on the skeleton, its discrete tangent (denoted by $\mathbf{t}(\mathbf{s}_i)$) can be evaluated by the centered difference with $\mathbf{s}_{i+1}$ and $\mathbf{s}_{i-1}$. Discrete version of the slope angle φ at $\mathbf{s}_i$ can be obtained by

$$\hat{\varphi} = |\theta(\mathbf{t}(\mathbf{s}_{i-1}), \mathbf{t}(\mathbf{s}_{i+1})) - \theta(\mathbf{t}(\mathbf{s}'_{i-1}), \mathbf{t}(\mathbf{s}'_{i+1}))| \tag{13}$$

with $\theta(\cdot)$ returning the angle between two vectors. The desired metric of bending elasticity at $\mathbf{s}_i$ can then be evaluated by

$$\hat{M}_\varphi = \hat{\varphi} / (\|\mathbf{s}_{i-1}\mathbf{s}_i\| + \|\mathbf{s}_i\mathbf{s}_{i+1}\|). \tag{14}$$

After getting $\hat{M}_\varphi$ and the diameter D determined in Section 5.1, the thickness of $\mathcal{C}$ can be determined by $t(D, M_\varphi)$. This value is then assigned to all sample points on $\mathcal{C}$.

The distribution of thicknesses given in the above way is very sparse (see the left of Fig.7). Moreover, a surface point could belong to different cross-sections, and therefore could be assigned with different values. According to the observation that bending is easy to happen at the thinnest place, the smallest one is selected when multiple values are assigned to a surface point. Then, the problem of sparsity is solved by interpolation. Specially, a continuous distribution of thicknesses is generated in a diffusion way by solving a Poisson equation, $\triangle t(\mathbf{p}) = 0$, subject to the values that have been assigned. Without loss of generality, the input model $\mathcal{H}$ is represented as a triangular mesh – a de facto standard file format for 3D printing. The desired thicknesses are assigned to every vertex on the mesh.

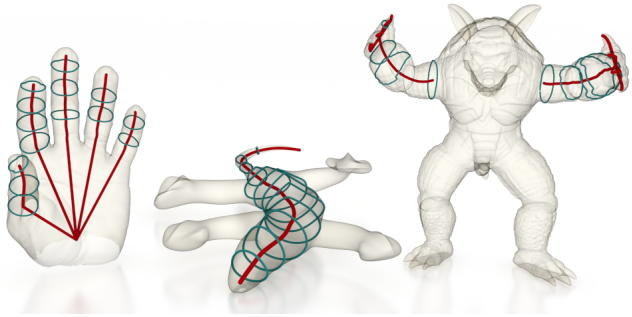

Figure 6: *The skeleton and virtual cross-sections are constructed on a few models for non-uniformly hollowing.*

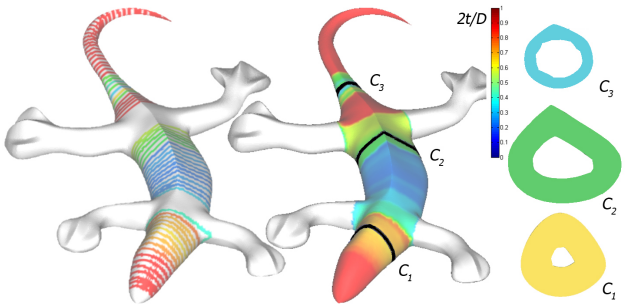

Figure 7: *Thicknesses diffusion – (left) thicknesses sparsely assigned according to cross-sections and (right) the interpolated thicknesses throughout the surface of a model.*

5.3. Non-uniform Hollowing

Uniformly hollowing of a given solid model is usually implemented by the offsetting operation, which is a well investigated problem in literature (e.g., [RR86, PK08]). However, non-uniform offsetting has been less studied. The interior surface of hollowing can be obtained by computing the boundary of sweeping, when sweeping the center of a sphere on the surface of $\mathcal{H}$. When dynamically changing the radius according to the thicknesses assigned at difference places, the boundary of sweeping presents the result of non-uniform hollowing. Nevertheless, computing such a general swept solid could be very time-consuming even after applying the hardware accelerated method [WM13].

An alternative method by using shifted distance-field is applied here to produce an approximation of the exact non-uniform hollowing. A distance-field, $d(\mathbf{p}, \partial\mathcal{H})$, evaluates the signed distances (inside *negative*) from any point $\mathbf{p} \in \Re^3$ to the surface of $\mathcal{H}$, $\partial\mathcal{H}$ is first constructed with the help of fast distance query [LGLM00]. The field-value is then shifted according to the distribution of thicknesses on $\mathcal{H}$ as follows:

$$d_s(\mathbf{p}, \partial\mathcal{H}) = d(\mathbf{p}, \partial\mathcal{H}) - t(\mathbf{q}(\mathbf{p})) \tag{15}$$

with $\mathbf{q}(\mathbf{p}) = arg\min \|\mathbf{q} - \mathbf{p}\|$ $(\forall \mathbf{q} \in \partial H)$. Finally, the interior surface of non-uniform hollowing can be extracted by *marching cubes* (MC) algorithm [LC87] for the zero isosurface $d_s(\mathbf{p}, \partial\mathcal{H}) = 0$. Note that as the shifting of distance-field does not guarantee a good ap-

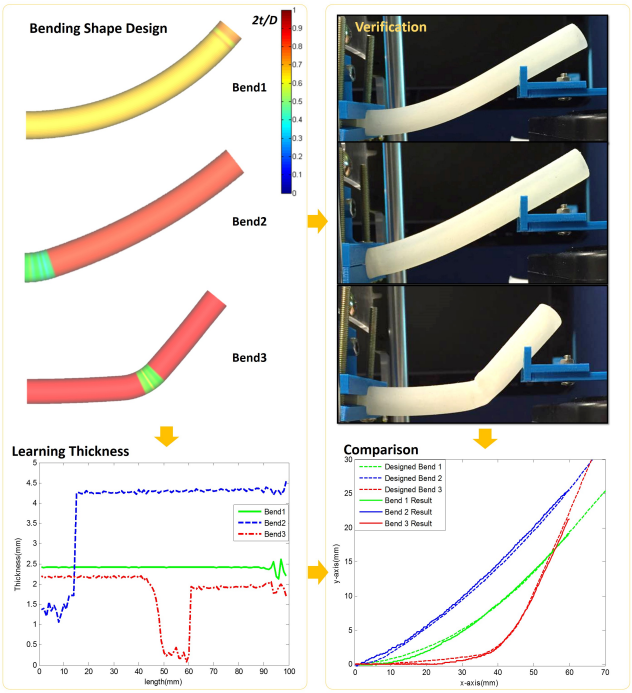

Figure 8: *Non-uniformly hollowed tubes for quantitative verification of our method: (left-top) designed different behaviors of bending, (right-top) physical models realized by 3D printing, (left-bottom) the computed distributions of thicknesses on three examples, and (right-bottom) comparisons on the shapes of skeletons on both designed and fabricated models.*

proximation by linear interpolation on the edges of cubes, the intersection between the isosurface and edges in MC is determined by the bi-sectional search. Moreover, the field-values are only assigned to a narrow-banded region around $\partial\mathcal{H}$ with distance not greater than $\max(t(\mathbf{p}))$ $(\forall \mathbf{p} \in \partial\mathcal{H})$.

6. Results

The method presented in this paper is verified on a few examples, where both simple models and free-form models are used. The non-uniformly hollowed models are fabricated by 3D printing on two different machines: Stratasys Connex3 – an industry-level machine and WiseMaker Pro W600 – a consumer-level device. The desired bending behaviors can be successfully realized by our method on physical models. The distribution of thicknesses can be generated in real-time as the function $t(\cdot)$ is formulated in closed-form. The computation of non-uniform hollowing can be completed in less than 4.5 seconds when we use a shifted distance-field with 256^3 grids on models with up to 43.3k triangles.

6.1. Verification on Tubes

Cylindrical tubes with non-uniform thicknesses are tested to verify our method in a quantitative way. First of all, the desired bending behaviors are given by specifying the different shapes of a cylinder's skeleton. From this input the distribution of thicknesses can be computed by the function $t(\cdot)$, learned through the data acquisition of material used for fabrication. As shown in the left of Fig.8, different distributions are computed according to different desired shapes in bending. Here, the newly deformed shape of a cylinder is generated by a geometry-oriented wire-deformation [SF98] for illustration purposes only. The models are then non-uniformly hollowed according to these distributions of thicknesses. The printed models are placed on the same device of data acquisition under the same loading (see the right-top of Fig.8). Photos of the deformed models are taken and points of the medial-axis are extracted by image processing. After scaling these points according to the length of cylinders, the curves of the medial-axis in bending can be generated and compared with the curves of desired bending. See the right-bottom of Fig.8, the bending results realized by our method on physical models (displayed in solid curves) match well to the desired bending behaviors (displayed in dash curves). The maximal deviations in y-direction on three tubes are 1.08%, 1.52% and 1.34% respectively with reference to their lengths.

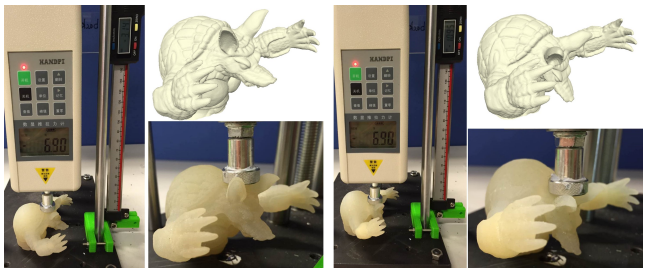

Figure 9: *Comparison of bending on models (left) with uniform thickness and (right) with varying thickness under the same loading.*

6.2. Models with Complex Shape

The effectiveness of the method presented in this paper is further validated on free-form models. The first example is the Armadillo model. As shown in Fig.1, the shell thickness can be used to design the deformation behaviors under the same loads applied on the two paws of the Armadillo. Both symmetric and asymmetric results can be generated. Another example is also shown in Fig.9 to demonstrate different deformations that can be generated on uniform and non-uniform hollowed Armadillos near the neck region when the same loading is applied.

In the example of the lizard model (see Fig.10), the user designs the desired skeleton's shape by dragging the points of the skeleton using the design interface, the colormaps for illustrating the distribution of thicknesses can be generated in real-time. After the designer confirms the skeletal shape in bending, the result of non-uniform hollowing can be produced immediately with the help of a shifted distance-field — see Fig.10 for both the distributions of thicknesses and the verification on printed models. Note that, although the MC algorithm is employed in our implementation, other polygonalization algorithms for tessellating an implicit surface can

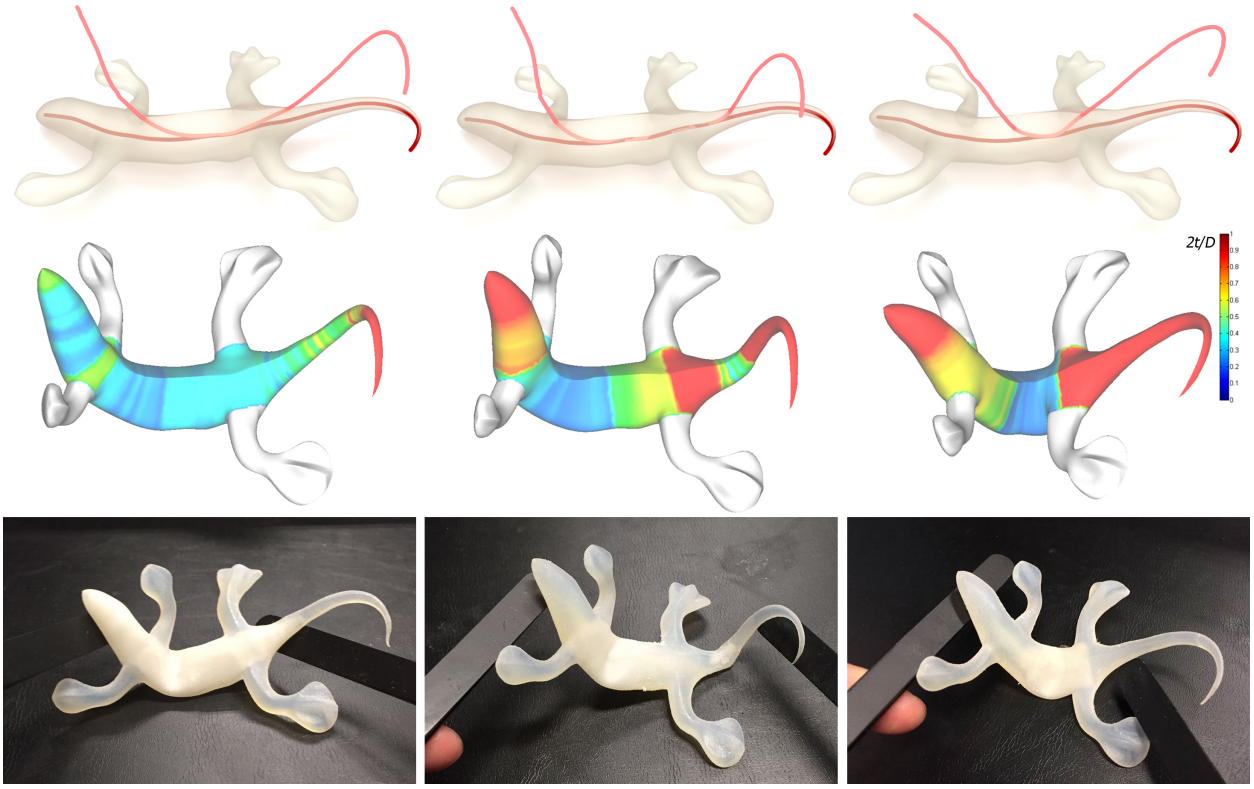

Figure 10: *Experimental results on a lizard model with different bending behavior specified by skeletons in different shapes (top row). The corresponding distributions of shell thicknesses are illustrated by colormaps with blue (minimum) and red (maximum) (middle row). The desired bending behaviors can be observed on the physical models fabricated by 3D printing (bottom row).*

also be applied here [JLSW02]. The resultant mesh surface must be water-tight and intersection-free so avoid causing any problem in the fabrication by 3D printing. Moreover, for the hollowing with a very thin shell, the resolution of distance-field computation needs to be refined to prevent intersection between the interior and exterior surfaces of a hollowed model.

The third example is a hand model tested on another 3D printer using a different material. The steps of data acquisition and learning need to be retaken. The tubes in different diameters/thicknesses are printed and tested to learning a new thickness function $t^*(\cdot)$ for this new material. After that, the newly learned function is applied to design the bending behaviors of a hand on different fingers. Deformation behaviors can be realized similar to articulated models with complex joint design, simply by using the change of thicknesses.

7. Discussion

In this paper, we introduce a framework to allow users to fabricate models having desired bending behaviors by 3D printing. Different bending behaviors are realized by changing shell thicknesses on an input model in generalized cylindrical shapes. A data-driven approach is developed to first acquire the bending behaviors of materials on tubes with different diameters and thicknesses. Then, the thickness function is constructed from the acquired data-set by ESN-based learning. The function can be applied to different models to supervise the non-uniform hollowing efficiently. The effectiveness of this method has been verified on models fabricated by different 3D printers, and the designed targets can be accurately matched on the physical deformation of models generated by our approach. In summary, our work provides a novel tool to design the deformation behavior of 3D printed models at interactive rates.

There are still unsolved problems to be investigated in future research. For a uniform tube, we approximate the curvature as constant locally so that the relative bending elasticity will not be affected by the length of cylinders. To achieve more accurate learning results, we could generate more training data by applying loads at different places on cylinders therefore different deflections can be measured to enhance the training set. Applying non-uniform hollowing can only make the bending stiffness weaker rather than enhancing the stiffness. It would be interesting to combine hollowing with exterior offsetting to enhance the stiffness at regions with small features [SVB*12, ZPZ13]. In another aspect, buckling can occur on thin shells under large deformation. Such phenomenon has caught researchers' attention in cloth simulation [CK02, WHRO10, UKIG11]. Our work can be further enhanced to introduce a better lower bound on the thickness of shells to avoid buckling in the design of bending elasticity. Last but not the least, the fabrication of hollowed models needs the help of inte-

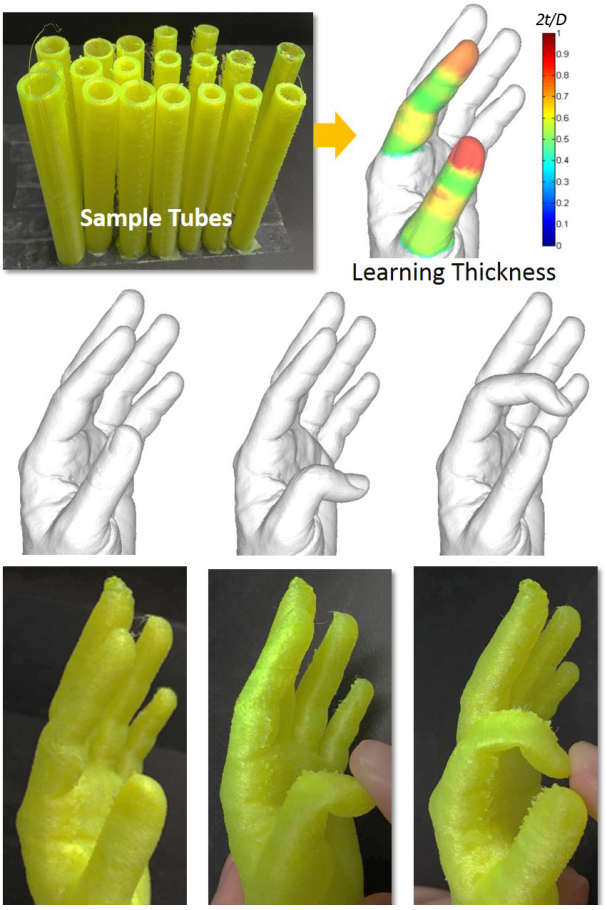

Figure 11: *An example using a new material and machine to realize the design of bending behaviors on different fingers of a hand model.*

rior supporting structures in 3D printing. The current practice is to manually remove those structure in a post-processing step. Methods to avoid generating interior supports is still a challenging and open problem.

References

[BBO*09] BICKEL B., BÄCHER M., OTADUY M. A., MATUSIK W., PFISTER H., GROSS M.: Capture and modeling of non-linear heterogeneous soft tissue. *ACM Transactions on Graphics (TOG) 28*, 3 (2009), 89. 2

[BBO*10] BICKEL B., BÄCHER M., OTADUY M. A., LEE H. R., PFISTER H., GROSS M., MATUSIK W.: Design and fabrication of materials with desired deformation behavior. *ACM Transactions on Graphics (TOG) 29*, 4 (2010), 63. 2

[BKS*12] BICKEL B., KAUFMANN P., SKOURAS M., THOMASZEWSKI B., BRADLEY D., BEELER T., JACKSON P., MARSCHNER S., MATUSIK W., GROSS M.: Physical face cloning. *ACM Trans. Graph. 31*, 4 (2012), 118:1–118:10. 2

[CK02] CHOI K.-J., KO H.-S.: Stable but responsive cloth. *ACM Trans. Graph. 21*, 3 (July 2002), 604–611. 8

[CLSM15] CHEN D., LEVIN D. I., SUEDA S., MATUSIK W.: Data-driven finite elements for geometry and material design. *ACM Transactions on Graphics (TOG) 34*, 4 (2015), 74. 2

[CSS06] CZICHOS H., SAITO T., SMITH L. R.: *Springer handbook of materials measurement methods*. Springer Science & Business Media, 2006. 1

[CZXZ14] CHEN X., ZHENG C., XU W., ZHOU K.: An asymptotic numerical method for inverse elastic shape design. *ACM Transactions on Graphics (TOG) 33*, 4 (2014), 95. 1, 2

[DASTH10] DE AGUIAR E., SIGAL L., TREUILLE A., HODGINS J. K.: Stable spaces for real-time clothing. In *ACM Transactions on Graphics (TOG)* (2010), vol. 29, ACM, p. 106. 2

[DLG13] DONG Y., LIN S., GUO B.: Fabricating spatially-varying subsurface scattering. In *Material Appearance Modeling: A Data-Coherent Approach*. Springer, 2013, pp. 153–171. 3

[FLS69] FEYNMAN R. P., LEIGHTON R. B., SANDS M.: *[Lectures on physics]; The Feynman lectures on physics. 2 (1969). Mainly electromagnetism and matter*. Addison-Wesley, 1969. 3

[HB00] HUGHES T. J., BELYTSCHKO T.: Nonlinear finite element analysis. *ICE Division, Zace Services Ltd* (2000). 4

[HFM*10] HAŠAN M., FUCHS M., MATUSIK W., PFISTER H., RUSINKIEWICZ S.: Physical reproduction of materials with specified subsurface scattering. In *ACM Transactions on Graphics (TOG)* (2010), vol. 29, ACM, p. 61. 3

[HSTP11] HILDEBRANDT K., SCHULZ C., TYCOWICZ C. V., POLTHIER K.: Interactive surface modeling using modal analysis. *ACM Transactions on Graphics (TOG) 30*, 5 (2011), 119. 2

[Jae01] JAEGER H.: *Short term memory in echo state networks*. GMD-Forschungszentrum Informationstechnik, 2001. 5

[Jae02] JAEGER H.: *Tutorial on training recurrent neural networks, covering BPPT, RTRL, EKF and the" echo state network" approach*. GMD-Forschungszentrum Informationstechnik, 2002. 5

[JLSW02] JU T., LOSASSO F., SCHAEFER S., WARREN J.: Dual contouring of hermite data. *ACM Trans. Graph. 21*, 3 (July 2002), 339–346. 8

[JSP*15] JEONG S., SOLENTHALER B., POLLEFEYS M., GROSS M., ET AL.: Data-driven fluid simulations using regression forests. *ACM Transactions on Graphics (TOG) 34*, 6 (2015), 199. 2

[KJ09] KIM T., JAMES D. L.: Skipping steps in deformable simulation with online model reduction. *ACM transactions on graphics (TOG) 28*, 5 (2009), 123. 2

[KMOD09] KHAREVYCH L., MULLEN P., OWHADI H., DESBRUN M.: Numerical coarsening of inhomogeneous elastic materials. *ACM Transactions on Graphics (TOG) 28*, 3 (2009), 51. 2

[KW13] KEITH T., WEDDELL S. J.: The echo state network on the graphics processing unit. In *Artificial Intelligence and Soft Computing* (2013), Springer, pp. 96–107. 5

[LC87] LORENSEN W. E., CLINE H. E.: Marching cubes: A high resolution 3d surface construction algorithm. *SIGGRAPH Comput. Graph. 21*, 4 (1987), 163–169. 6

[LDPT13] LAN Y., DONG Y., PELLACINI F., TONG X.: Bi-scale appearance fabrication. *ACM Transactions on Graphics (TOG) 32*, 4 (2013), 145. 3

[LGLM00] LARSEN E., GOTTSCHALK S., LIN M., MANOCHA D.: Fast distance queries with rectangular swept sphere volumes. In *Robotics and Automation, 2000. Proceedings. ICRA '00. IEEE International Conference on* (2000), vol. 4, pp. 3719–3726 vol.4. 6

[LSWW14] LIU L., SHAMIR A., WANG C., WHITENING E.: 3d printing oriented design: Geometry and optimization. In *SIGGRAPH Asia 2014 Courses* (New York, NY, USA, 2014), SA '14, ACM. 2

[LSZ*14] LU L., SHARF A., ZHAO H., WEI Y., FAN Q., CHEN X., SAVOYE Y., TU C., COHEN-OR D., CHEN B.: Build-to-last: Strength to weight 3d printed objects. *ACM Transactions on Graphics (TOG) 33*, 4 (2014), 97. 3

[LYS11] LIN X., YANG Z., SONG Y.: Intelligent stock trading system based on improved technical analysis and echo state network. *Expert systems with Applications 38*, 9 (2011), 11347–11354. 5

[MAB*15] MUSIALSKI P., AUZINGER T., BIRSAK M., WIMMER M., KOBBELT L.: Reduced-order shape optimization using offset surfaces. *ACM Trans. Graph 34*, 4 (2015), 102. 3

[MAG*09] MATUSIK W., AJDIN B., GU J., LAWRENCE J., LENSCH H., PELLACINI F., RUSINKIEWICZ S.: Printing spatially-varying reflectance. In *ACM Transactions on Graphics (TOG)* (2009), vol. 28, ACM, p. 128. 3

[MBT*12] MIGUEL E., BRADLEY D., THOMASZEWSKI B., BICKEL B., MATUSIK W., OTADUY M. A., MARSCHNER S.: Data-driven estimation of cloth simulation models. In *Computer Graphics Forum* (2012), vol. 31, Wiley Online Library, pp. 519–528. 2

[MHR*16] MUSIALSKI P., HAFNER C., RIST F., BIRSAK M., WIMMER M., KOBBELT L.: Non-linear shape optimization using local subspace projections. *ACM Transactions on Graphics* (2016). 3

[MTGG11] MARTIN S., THOMASZEWSKI B., GRINSPUN E., GROSS M.: Example-based elastic materials. *ACM Transactions on Graphics (TOG) 30*, 4 (2011), 72. 2

[NMK*06] NEALEN A., MÜLLER M., KEISER R., BOXERMAN E., CARLSON M.: Physically based deformable models in computer graphics. In *Computer Graphics Forum* (2006), vol. 25, Wiley Online Library, pp. 809–836. 2

[PK08] PAVIC D., KOBBELT L.: High-Resolution Volumetric Computation of Offset Surfaces with Feature Preservation. *Computer Graphics Forum* (2008). 6

[PLR*16] PIOVARČI M., LEVIN D. I., REBELLO J., CHEN D., ĎURIKOVIČ R., PFISTER H., MATUSIK W., DIDYK P.: An interaction-aware, perceptual model for non-linear elastic objects. *ACM Transactions on Graphics (Proc. SIGGRAPH) 35*, 4 (2016). 2

[PTC*15] PÉREZ J., THOMASZEWSKI B., COROS S., BICKEL B., CANABAL J. A., SUMNER R., OTADUY M. A.: Design and fabrication of flexible rod meshes. *ACM Transactions on Graphics (TOG) 34*, 4 (2015), 138. 3

[PWLSH13] PRÉVOST R., WHITING E., LEFEBVRE S., SORKINE-HORNUNG O.: Make it stand: balancing shapes for 3d fabrication. *ACM Transactions on Graphics (TOG) 32*, 4 (2013), 81. 3

[PZM*15] PANETTA J., ZHOU Q., MALOMO L., PIETRONI N., CIGNONI P., ZORIN D.: Elastic textures for additive fabrication. *ACM Transactions on Graphics (TOG) 34*, 4 (2015), 135. 2, 3

[RR86] ROSSIGNAC J. R., REQUICHA A. A. G.: Offsetting operations in solid modelling. *Comput. Aided Geom. Des. 3*, 2 (Aug. 1986), 129–148. 6

[SB12] SIFAKIS E., BARBIC J.: Fem simulation of 3d deformable solids: a practitioner's guide to theory, discretization and model reduction. In *ACM SIGGRAPH 2012 Courses* (2012), ACM, p. 20. 2

[SBR*15] SCHUMACHER C., BICKEL B., RYS J., MARSCHNER S., DARAIO C., GROSS M.: Microstructures to control elasticity in 3d printing. *ACM Transactions on Graphics (TOG) 34*, 4 (2015), 136. 1, 2, 3

[SF98] SINGH K., FIUME E.: Wires: A geometric deformation technique. In *Proceedings of the 25th Annual Conference on Computer Graphics and Interactive Techniques* (New York, NY, USA, 1998), SIGGRAPH '98, ACM, pp. 405–414. 7

[SSW*13] STOOP R., SAASE V., WAGNER C., STOOP B., STOOP R.: Beyond scale-free small-world networks: cortical columns for quick brains. *Physical review letters 110*, 10 (2013), 108105. 5

[STC*12] SCHUMACHER C., THOMASZEWSKI B., COROS S., MARTIN S., SUMNER R., GROSS M.: Efficient simulation of example-based materials. In *Proceedings of the ACM SIGGRAPH/Eurographics Symposium on Computer Animation* (2012), Eurographics Association, pp. 1–8. 2

[STC*13] SKOURAS M., THOMASZEWSKI B., COROS S., BICKEL B., GROSS M.: Computational design of actuated deformable characters. *ACM Transactions on Graphics (TOG) 32*, 4 (2013), 82. 2

[SVB*12] STAVA O., VANEK J., BENES B., CARR N., MĚCH R.: Stress relief: improving structural strength of 3d printable objects. *ACM Transactions on Graphics (TOG) 31*, 4 (2012), 48. 3, 8

[TZCO09] TAGLIASACCHI A., ZHANG H., COHEN-OR D.: Curve skeleton extraction from incomplete point cloud. In *ACM Transactions on Graphics (TOG)* (2009), vol. 28, ACM, p. 71. 5

[UKIG11] UMETANI N., KAUFMAN D. M., IGARASHI T., GRINSPUN E.: Sensitive couture for interactive garment modeling and editing. *ACM Trans. Graph. 30*, 4 (July 2011), 90:1–90:12. 8

[UKSI14] UMETANI N., KOYAMA Y., SCHMIDT R., IGARASHI T.: Pteromys: interactive design and optimization of free-formed free-flight model airplanes. *ACM Transactions on Graphics (TOG) 33*, 4 (2014), 65. 3

[US13] UMETANI N., SCHMIDT R.: Cross-sectional structural analysis for 3d printing optimization. *SIGGRAPH Asia* (2013), 5. 3

[WHRO10] WANG H., HECHT F., RAMAMOORTHI R., O'BRIEN J. F.: Example-based wrinkle synthesis for clothing animation. In *ACM Transactions on Graphics (TOG)* (2010), vol. 29, ACM, p. 107. 2, 8

[WM13] WANG C. C. L., MANOCHA D.: Gpu-based offset surface computation using point samples. *Comput. Aided Des. 45*, 2 (Feb. 2013), 321–330. 6

[WOR11] WANG H., O'BRIEN J. F., RAMAMOORTHI R.: Data-driven elastic models for cloth: modeling and measurement. *ACM Transactions on Graphics (TOG) 30*, 4 (2011), 71. 2

[WPMR09] WEYRICH T., PEERS P., MATUSIK W., RUSINKIEWICZ S.: Fabricating microgeometry for custom surface reflectance. In *ACM Transactions on Graphics (TOG)* (2009), vol. 28, ACM, p. 32. 3

[WWY*13] WANG W., WANG T. Y., YANG Z., LIU L., TONG X., TONG W., DENG J., CHEN F., LIU X.: Cost-effective printing of 3d objects with skin-frame structures. *ACM Transactions on Graphics (TOG) 32*, 6 (2013), 177. 3

[WWY*15] WANG B., WU L., YIN K., ASCHER U., LIU L., HUANG H.: Deformation capture and modeling of soft objects. *ACM Transactions on Graphics (TOG) 34*, 4 (2015), 94. 2

[XLCB15] XU H., LI Y., CHEN Y., BARBIVČ J.: Interactive material design using model reduction. *ACM Transactions on Graphics (TOG) 34*, 2 (2015), 18. 2

[ZLP*15] ZHANG X., LE X., PANOTOPOULOU A., WHITING E., WANG C. C.: Perceptual models of preference in 3d printing direction. *ACM Transactions on Graphics (TOG) 34*, 6 (2015), 215. 3

[ZPZ13] ZHOU Q., PANETTA J., ZORIN D.: Worst-case structural analysis. *ACM Trans. Graph. 32*, 4 (July 2013), 137:1–137:12. 8

[ZYH*15] ZHOU Y., YIN K., HUANG H., ZHANG H., GONG M., COHEN-OR D.: Generalized cylinder decomposition. *ACM Transactions on Graphics (TOG) 34*, 6 (2015), 171. 5

[ZYZZ] ZHANG Y., YIN C., ZHENG C., ZHOU K.: Computational hydrographic printing. *To appear in ACM TOG 34*, 4. 3